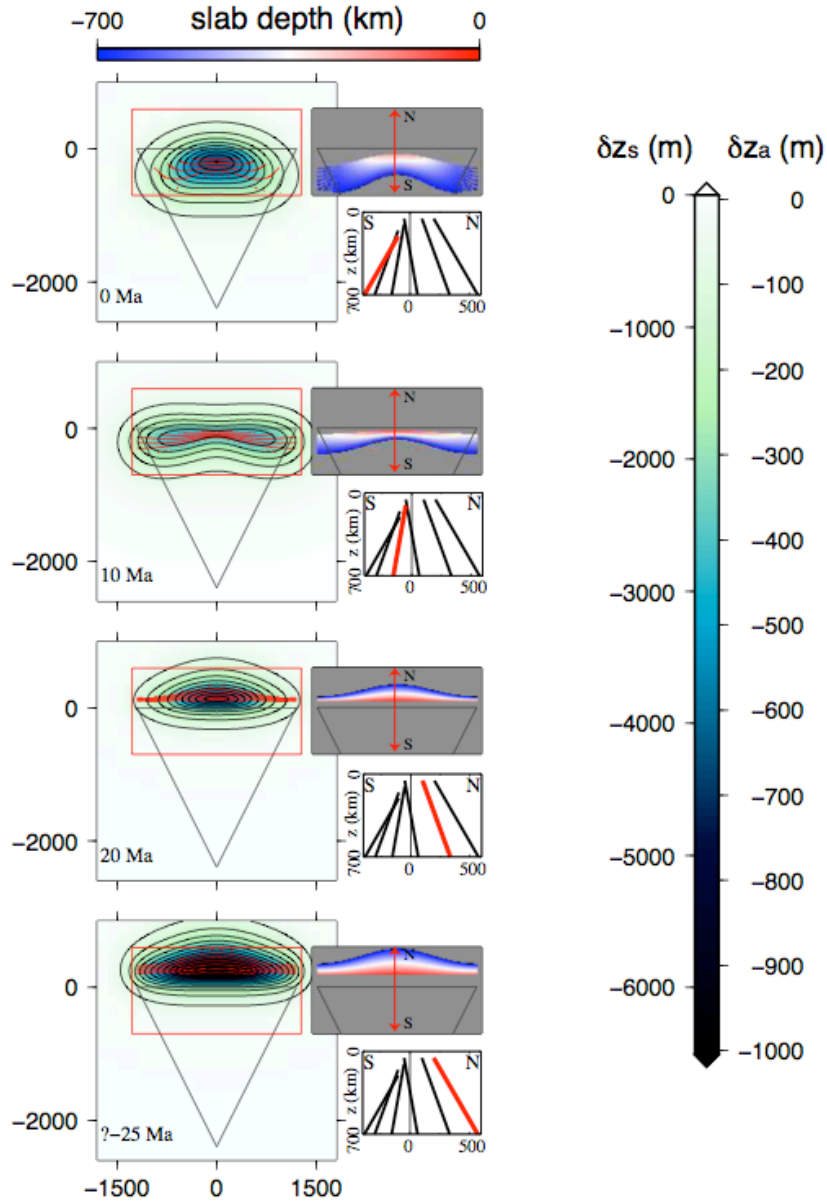


**Item DR1: Reconstruction method for the Indian slab geometry during the Neogene**

In order to reconstruct the morphology of the Indian slab through time, we built upon the work of Replumaz et al. (2010), wherein its geometry is inferred from an interpretation of the seismic tomography model of Li et al. (2008), together with kinematic considerations on the vertical sinking rate into the mantle. In this paper, they showed that the slab between Nepal and Makran is detached from the upper plate in Nepal and that the corresponding tear increases westward, following its onset at ~15 Ma. Here, we pursue and expand their analysis along the same lines by first visually exploring a variety of seismic tomography models (either P-wave, e.g. Li et al., 2008; Bijwaard et al., 1998; or S-wave, e.g. Becker and Boschi, 2002; Ritsema et al., 2011, or Debayle and Ricard, 2012) in order to locate the high wave speed bodies in the mantle at present-day. Second, surface kinematics reconstructions (as in e.g. Replumaz et al., 2010) further helps to interpret seismic tomography, and we propose that the slab is currently similarly stretched on both edges, because it remained anchored into the deeper mantle on the one hand, and because it is on the other hand attached to its lateral counterparts that normally subduct underneath Makran, to the West, and Sunda, to the East, that did not suffer from the indentation of the Indian continent. The forward (northward) migration of the trench, together with the northward progradation of the slab is rendered easier in the center, away from these continuing oceanic subductions.

Third, we speculate on the past geometries of the Indian slab by assuming a forward subduction of the Indian slab at 30 Ma, along the northern edge of the subducting greater India (e.g.

Replumaz et al., 2009; Capitanio et al., 2010). At 30 Ma, we assign to the slab a smooth morphology that would adapt to the shape of the inferred trench geometry based on kinematic reconstructions. Interpretations of analogue (Bajolet et al., 2013) and numerical (Capitanio et al., 2013) mechanical models further help to define the path that connects the initially regular subduction at ~30 Ma to the present-day geometry of the southward flipped Indian slab. Note that the timing of our reconstructions slightly departs from the scenario of Replumaz et al (2010). Indeed, we reappraise the kinematic model in order to preserve the best consistency with surface kinematics while keeping a relatively constant pace of slab stretching (or at least to prevent sudden accelerations or decelerations). This reconstruction is currently difficult to perform automatically, for backwards advection schemes are unfortunately not always trustworthy yet and can't integrate much of the geological record and experience that results from a variety of physical models abundantly published in the literature. Last, we reconstructed our idealized geometries in order to model the flow through time around the subducting slab and predict the associated dynamic deflections of the surface (Fig. DR1). Again, for the sake of clarity in this idealized model of the Indian convergence, the folding slab is implemented as gradually changing polarity. This further simplifies the geometry of the zone without altering significantly the mantle flow (and therefore the dynamic topography), as the density anomalies remain approximately distributed accordingly.



47

48 Figure DR1. Map views of the dynamic topography for an idealized Indian-Eurasian  
 49 convergence at 10 m.y. time steps. Scale metrics are either air- ( $\delta z_a$ ) or sediment- ( $\delta z_s$ )  
 50 compensated (500 m  $\delta z_s$  isocontours). Red contours: slab 100 km isocontours. Black triangle  
 51 delineates an idealized India. Insets: map views (color coded) and mid-sections (bars) of the  
 52 input reconstructed slab morphologies.

53

54

## 55 **Item DR2: Modeling dynamic topography**

56 We model the viscous flow underneath the Indian-Eurasian convergence zone following the

57 convenient *Stokeslets* approximation (Morgan, 1965; Harper, 1984). The density field is

58 discretized into point masses, and each point mass  $i$  induces an elementary flow for which the

59 stream function is known (e.g. Batchelor, 1967) and writes  $\psi_i = \frac{\Delta \rho v_i g}{8\pi \eta} r_{ij} \sin^2 \theta_{ij}$ , where

60  $\Delta \rho v_i$  is the mass anomaly associated with each point mass,  $g$  is the acceleration of gravity,

61  $\eta$  the viscosity,  $r_{ij}$  the distance from the point mass  $i$  to a point  $j$  at the surface, and  $\theta_{ij}$  the angle

62 between the vector  $ij$  and  $g$ . The normal stress is computed following the image technique, as in

63 Morgan (1965), such that  $F_{ij} = \frac{3 \Delta \rho v_i g z_i^3}{\pi r_{ij}^5}$ , where  $z_i$  is the depth of the point mass. For a stress

64 free surface, that normal stress shall be compensated by an opposite surface load. That surface

65 load is a deflection of the surface (dynamic topography)  $h_{ij} = \frac{F_{ij}}{(\rho_m - \rho) g}$ , where  $\rho_m$  is the density

66 of the mantle,  $\rho$  is the density of water in immersed domains, air in subaerial domains (as in the

67 Himalaya for instance) or sediments in sedimentary plains (like the Indo-Gangetic plain). The

68 total deflection  $H_{ij}$  is the sum of all individual deflections, such that the dynamic topography at

69 a given location is given by  $H_{ij} = \frac{3 \Delta \rho v_i g z_i^3}{\pi r_{ij}^5 (\rho_m - \rho)}$ . This approximation has proven succesful in

70 global (e.g. Ricard et al., 1993) or more regional models. Here, we take advantage of that

71 formalism to explore dynamic topography as in Husson (2006) first above a flowing mantle

72 whose density field is inferred from seismic tomography, and second above a theoretical flowing

73 mantle around reconstructed idealized slab geometries.

At present-day, dynamic topography and its time-dependence can be approximated thanks to mantle flow models derived from seismic tomography, either globally (e.g. Forte et al., 1993; Gurnis et al., 2000; Conrad and Husson, 2009; Steinberger, 2007), or more locally, where the density anomalies that are located in the upper mantle generate short wavelength, high amplitude deflections of the surface of the Earth that successfully explain a variety of surface observables (e.g. Husson, 2006; Guillaume et al., 2009, 2013; Dávila and Lithgow-Bertelloni, 2010). Deriving mantle flow from seismic tomography nevertheless requires a set of assumptions to convert seismic anomalies into densities and rheologies, and to build a consistent setup. Such approximations are either complex (e.g. Simmons et al., 2009) or simple (here). Both approaches equally face the poor knowledge that we have on the Earth rheology, we thus opt for simplicity and conveniently adapt the *Stokeslets* approximation. We convert P-wave velocity anomalies from Li and Van der Hilst (2008) into a 3D field of density anomalies using a linear conversion between seismic wavespeed anomaly and densities, such that  $\Delta\rho=14 \text{ kg m}^{-3} / \% \Delta_{VP}$  (comparable to those found in Husson, 2006; or Conrad and Behn, 2010, or Husson et al., 2012). Tuning this value scales the magnitude of the deflections, as well as the density contrast between the mantle and the filling material, i.e. sediments in the Indo-Gangetic plain (here set to  $\rho_m - \rho = 500 \text{ kg m}^{-3}$ ), air in the Himalayan belt (set to  $\rho_m - \rho = 3200 \text{ kg m}^{-3}$ ). We therefore predict air-compensated deflections  $\delta z_a$  as well as sediment-compensated deflections  $\delta z_s$ .

We similarly computed models of dynamic topography from our reconstructed geometries at intervals of 5 myrs. Slabs at each time steps are accordingly discretized into individual *Stokeslets*. The negative buoyancy of the slab at any time is computed assuming that an unstretched section has a thickness of 110 km and a density contrast with the mantle of  $60 \text{ kg m}^{-3}$ . The total buoyancy of the slab in the upper mantle is assumed uniform per unit trench length

at each time step. But because it is stretched as it gets closer to the edges, its thickness decreases, and so is the absolute buoyancy of the individual point masses, that we modify accordingly. In these models, we only consider the density anomaly of the slab; henceforth the net density anomaly is positive. In only implicitly corresponds to the assumptions that the opposite buoyancy anomalies (to restore a neutral net buoyancy) is either uniformly distributed in the mantle or too far away to produce any effect in the area. In both cases, it therefore has no impact on the model predictions. Again, we make predictions of air-compensated deflections  $\delta z_a$  as well as sediment-compensated deflections  $\delta z_s$  at each time-step.

## REFERENCES CITED

Batchelor, G., 1967, An Introduction to Fluid Mechanics, Cambridge University Press.

Bajolet, F., Replumaz, A., Lainé, R., 2013, Orocline and syntaxes formation during subduction and collision, *Tectonics*, v. 32, p. 1529-1546.

Becker, T.W., and Boschi, L., 2002, A comparison of tomographic and geodynamic mantle models, *Geochem., Geophys., Geosyst.*, v. 3, doi:10.1029/2001GC000168.

Capitanio, F.A., Morra, G., Goes, S., Weinberg, R.F. and Moresi, L., 2010, India-Asia convergence driven by the subduction of the Greater Indian continent, *Nature Geoscience*, doi: 10.1038/NGEO725.

120

121 Capitanio, F.A. and Replumaz A., 2013, Subduction and slab breakoff controls on Asian  
122 Indentation tectonics and Himalayan Western Syntaxis formation, *Geochem. Geophys.*  
123 *Geosyst.*, doi: 10.1002/ggge.20171.

124

125 Conrad, C.P., and Behn, M.D., 2010. Constraints on lithosphere net rotation and asthenospheric  
126 viscosity from global mantle flow models and seismic anisotropy. *Geochem. Geophys. Geosyst.*  
127 11, doi:10.1029/2009GC002970.

128

129 Conrad, C.P., and Husson, L., 2009, Influence of dynamic topography on sea level and its rate of  
130 change, *Lithosphere*, v. 1, p. 110-120.

131

132 Dávila, F.M., Lithgow-Bertelloni, C., Giménez, M., 2010, Tectonic and dynamic controls on the  
133 topography and subsidence of the Argentine Pampas: the role of the flat slab, *Earth and Planetary*  
134 *Science Letters*, v. 295, p. 187–194.

135

136 Debayle, E., and Ricard, Y., 2012, A global shear velocity model of the upper mantle from  
137 fundamental and higher Rayleigh mode measurements, *J. Geophys. Res.*, v. 117,  
138 doi:10.1029/2012JB009288.

139

140 Forte, A.M., Peltier, W.R., Dziewonski, A.M. and Woodward, R.L., 1993, Dynamic surface  
141 topography: A new interpretation based upon mantle flow models derived from seismic  
142 tomography. *Geophys. Res. Lett.*, v. 20, doi: 10.1029/93GL00249.

143

144 Guillaume, B., Martinod, J., Husson, L., Roddaz, M., Riquelme, R., 2009, Neogene uplift of  
 145 central-eastern Patagonia: dynamic response to active spreading-ridge subduction?, *Tectonics*, v.  
 146 28, doi:10.1029/2008TC002324.  
 147  
 148 Guillaume, B., Gautheron, C., Simon-Labric, T., Martinod, J., Roddaz, M., Douville, E., 2013,  
 149 Dynamic topography control on Patagonian relief evolution as inferred from low temperature  
 150 thermochronology, *Earth and Planetary Science Letters*, v. 364, p. 157-167.  
 151  
 152 Gurnis, M., Mitrovica, J.X., Ritsema, J., and van Heijst, H.J., 2000, Constraining mantle density  
 153 structure using geological evidence of surface uplift rates: The case of the African Superplume,  
 154 *Geochem. Geophys. Geosyst.*, v. 1, doi:10.1029/1999GC000035.  
 155  
 156 Husson, L., 2006: Dynamic topography above retreating subduction zones, *Geology*, v. 34, p.  
 157 741-744.  
 158  
 159 Husson, L., Conrad, C.P., and Faccenna, C., 2012, Plate motions, Andean orogeny, and  
 160 volcanism above the South Atlantic convection cell, *Earth Planet Sci. Lett.*,  
 161 doi:10.1016/j.epsl.2011.11.040.  
 162  
 163 Harper, J.F., 1984, Mantle flow due to internal vertical forces: *Physics of the Earth and Planetary*  
 164 *Interiors*, v. 36, p. 285–290.  
 165



166 Li, C., Van der Hilst, R.D., Engdahl, E.R., and Burdick, S., 2010, A new global model for P-  
 167 wavespeed variations in Earth's mantle, *Geochem. Geophys. Geosy.*, v. 9,  
 168 doi:10.1029/2007GC001806.  
 169  
 170 Morgan, W., 1965, Gravity anomalies and convection currents: *Journal of Geophysical Research*,  
 171 v. 70, p. 6175–6187.  
 172  
 173 Replumaz A., Negredo A.M., Guillot S. and Villaseñor A., 2010, Multiple episodes of  
 174 continental subduction during India/Asia convergence: insight from seismic tomography and  
 175 tectonic reconstruction, *Tectonophysics*, 483, p. 125-134.  
 176  
 177 Replumaz A., Negredo A.M., Guillot S. and Villaseñor A., 2009 Multiple episodes of continental  
 178 subduction during India/Asia convergence: insight from seismic tomography and tectonic  
 179 reconstruction, *Tectonophysics*, v. 483, p. 125-134.  
 180  
 181 Ritsema J, van Heijst HJ, Deuss A, and Woodhouse JH, S40RTS, 2011, A degree-40 shear-  
 182 velocity model for the mantle from new Rayleigh wave dispersion, teleseismic traveltimes,  
 183 and normal-mode splitting function measurements, *Geophys. J. Int.*, v. 184,  
 184 doi:10.1111/j.1365–246X.2010.04884.x.  
 185  
 186 Simmons, N.A., Forte, A.M., Boschi, L., Grand, S.P., 2010, GyPSuM: A joint tomographic  
 187 model of mantle density and seismic wave speeds, *Journal of Geophys. Res.*, v. 115.,  
 188 doi:10.1029/2010JB007631.

189

190 Steinberger, B., 2007, Effect of latent heat release at phase boundaries on flow in the Earth's  
191 mantle, phase boundary topography and dynamic topography at the Earth's surface, *Phys. Earth*  
192 *Planet. Inter.*, v. 164, p. 2-20.

193